Modeling Repeatedly Flaring δ Sunspots

Piyali Chatterjee,[1,2,*] Viggo Hansteen,[1] and Mats Carlsson[1]
[1]Institute of Theoretical Astrophysics, University of Oslo, P.O. Box 1029 Blindern, N-0315 Oslo, Norway
[2]Indian Institute of Astrophysics, II Block Koramangala, Bengaluru-560034, India
(Received 23 September 2015; published 7 March 2016)

Active regions (ARs) appearing on the surface of the Sun are classified into α, β, γ, and δ by the rules of the Mount Wilson Observatory, California on the basis of their topological complexity. Amongst these, the δ sunspots are known to be superactive and produce the most x-ray flares. Here, we present results from a simulation of the Sun by mimicking the upper layers and the corona, but starting at a more primitive stage than any earlier treatment. We find that this initial state consisting of only a thin subphotospheric magnetic sheet breaks into multiple flux tubes which evolve into a colliding-merging system of spots of opposite polarity upon surface emergence, similar to those often seen on the Sun. The simulation goes on to produce many exotic δ sunspot associated phenomena: repeated flaring in the range of typical solar flare energy release and ejective helical flux ropes with embedded cool-dense plasma filaments resembling solar coronal mass ejections.

DOI: 10.1103/PhysRevLett.116.101101

δ sunspots are formed when two sunspots of opposite polarity magnetic field appear very close to each other and reside in the same penumbra, the radial filamentary structure outside the umbral region of the strongest magnetic fields. Strong shear and horizontal magnetic fields often exist at the polarity-inversion line separating the two polarities [1]. The subsurface processes which form the δ sunspots are still debated. Early observational studies [2,3] propose that δ sunspots form from the collision merging of topologically separate dipoles, while numerical simulations by Refs. [4,5] show that a kink unstable magnetic flux-tube —helical field lines winding around a central axis— emerging from the subsurface can have a δ sunspot-like structure. More recently, attempts to model the δ spot in the NOAA AR 11158 utilized a uniformly twisted subsurface flux tube initially buoyant in two adjacent regions along its length [6,7]. Also, Ref. [8] found a magnetic flux concentration resembling a δ sunspot in their stratified helical dynamo simulation. These studies did not report any flaring activity. On the other hand, Ref. [9] initialized their simulation with two parallel flux tubes each lying at a different depth from the surface and with a different value of the initial magnetic twist which later evolved into a δ sunspot-like structure and powered multiple reconnection events. δ sunspots are highly flare productive—95% of the strongest (X-class) x-ray flares originate from these regions [3]. Using a realistic numerical simulation [10] showed that interaction between adjacent expanding magnetic bipoles pressing against each other can lead to the formation of strong current layers in the atmosphere which in turn lead to repeated flaring in the region. Here, we report on a three-dimensional magnetohydrodynamic (MHD) simulation of the formation of a δ sunspot-like region as a result of the breakup of a cool magnetic layer embedded in the upper solar convection zone into several flux tubes due to the growth of three-dimensional unstable modes excited in the layer. This instability is well known in the literature as the undular instability (UI) [11,12]. The magnetic layer initially inserted is thinner than the local pressure scale height —a precondition for UI. A detailed study of UI was performed by Refs. [13,14] in a very similar setup but without convection. They also calculated the amount of magnetic twist that is generated by the UI inside a thin magnetic layer with zero initial twist in a stratified, and rotating plasma. The latter study also found that the tubes formed are more twisted with increasing rotation. Also, the sign of the mean twist in the domain changes with the sense of the rotation vector. As it is not yet possible to observationally discern the subsurface structure of the sunspots, most simulations so far employ only uniformly twisted kink-unstable cylindrical flux tubes as the initial condition. The amount of twist applied is a free parameter and so are the segments where the tubes must be initially buoyant. Our simple initial condition alleviates the need for such free parameters.

We solve the equations of compressible magnetohydrodynamics in a 36 Mm $\times$ 36 Mm $\times$ 25 Mm Cartesian box using the higher-order finite difference code, the Pencil Code [15]. The box rotates with a solarlike angular velocity $\Omega = 2.59 \times 10^{-6}$ s^{-1} making an angle of 30° with the vertical z direction. The box is resolved using a uniformly spaced grid with $dx = dy = 96$ km and $dz = 48$ km. The initial state is a convectively relaxed state with the vertical profiles of density, ρ, and temperature, T, given by Fig. 1(a). The domain consists of a subphotospheric superadiabatic layer in the lower 8.5 Mm of the box. The layer above ($0 < z < 2$ Mm) is cooled by a radiative cooling term $\propto \rho^2 \Lambda(T)$ in the entropy equation to drive the

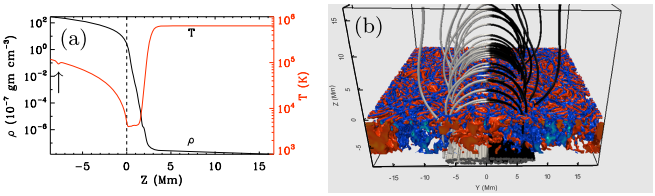

FIG. 1. (a) Vertical profiles of the horizontal averages of initial density and temperature. The arrow indicates the position of the cool magnetic sheet. (b) Initial magnetic field lines shaded black (white) indicating positive (negative) B_z. The isosurfaces of the upward (red) and the downward (blue) velocity in the convective layer highlights the granulation pattern.

surface convection and mimic the photosphere and the chromosphere. The temperature in this layer connects via a transition region to an isothermal corona (3.5 Mm $< z <$ 16.5 Mm) maintained at 8.0×10^5 K by a Newtonian *cooling* term. Into this steady state atmosphere we introduce a horizontal magnetic sheet at $z_0 = -7.75$ Mm with the magnetic field vector, **B**, strongly oriented in the x direction as shown in Fig. 1(b). The horizontal extent of the sheet is about -3 Mm $< y < 3$ Mm and the maximum half-width, R, is 0.3 Mm at $y = 0$. The sheet is neutrally buoyant with respect to the surroundings to prevent it from rising immediately. However, to maintain magnetostatic equilibrium we cool it by reducing the specific entropy inside the sheet. The initial plasma-β, which is the ratio of gas pressure to magnetic pressure is ~0.6. Simulations of the generation of such a magnetic sheet due to dynamo action and its subsequent breakup into buoyant flux tubes have been performed [16]. It is also likely that the apex of an Ω-shaped ribbon rising from deep inside the convection zone as in Fig. 3(b) of Ref. [17] can be described in terms of such a sheet. Furthermore, we introduce an ambient magnetic field in the form of a potential field arcade at $z > 0$ also shown in Fig. 1(b) to facilitate the perturbations formed due to the insertion of the strong magnetic sheet to travel along the field lines and out of the domain. Initially, the magnetic field at the photospheric foot points of the parallel arcade is 10 G. The lower boundary at $z = -8.5$ Mm is closed whereas the upper boundary only allows mass outflow with a vertical magnetic field condition. The x boundaries are periodic, while the y boundaries are perfectly conducting walls. Further details about the MHD equations, initial conditions, and the dissipation coefficients used here are given in Ref. [18].

Our numerical simulation was run for 263 min of solar time. We show the breaking up of the magnetic sheet into tubes and its subsequent evolution in Figs. 2(a)–2(b) using volume rendering of a scalar quantity $B\rho^{-1/4}$, where B is the magnetic field strength. Here, the subsurface convection excites several spatial modes at the onset of the UI. As a result, the wave number along x is between one and two and the wave number in y is larger than twelve, which is the number of tubes counted from panel (b). The dominant

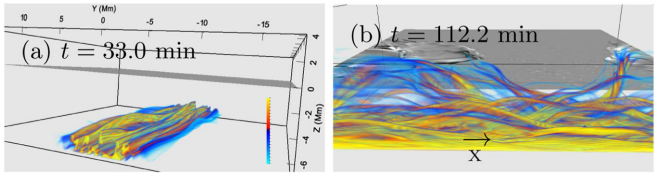

FIG. 2. Volume rendering of the quantity $B\rho^{-1/4}$ at times indicated in the figure. The gray shaded surface represents B_z in the $z = 0$ layer.

mode excited will likely depend on the aspect ratio of the initial magnetic sheet as well as on the boundary conditions in the x direction. The magnetic field strength inside the newly formed flux tubes at $z = -7.75$ Mm is about 25 kG. Figure 2(b) depicts the progenitors of the δ sunspot as separate fronts of positive and negative B_z emerging at $z = 0$ which successively move closer. The progenitors consist of different flux systems even though we traced some field lines directly connecting the spots below the photosphere. Figure 3 shows snapshots of the photospheric vertical magnetic field before and after the formation of the δ sunspot region upon collision of the opposite polarities of similar sizes and magnetic field strength. The unsigned magnetic flux emerging into the black square reaches a maximum of 7.25×10^{20} Mx at $t = 200$ min and decreases slightly thereafter. The threadlike patterns of mixed polarities seen on both sides of the δ sunspot in the photospheric magnetogram indicate that there are two emerging and expanding bipolar regions side by side, the lateral extremes of which may be imagined to go beyond the periodic x boundaries. The collision is marked by several flares. A solar flare occurs when magnetic energy is suddenly released in the form of heat, radiation, and energetic particle emission inside very thin current sheets—that are regions of very strong magnetic field gradients and thus sites where the magnetic field topology undergoes a major change. These flares thus reconnect field lines, ultimately leading to the components of the δ sunspot becoming increasingly directly connected by field lines

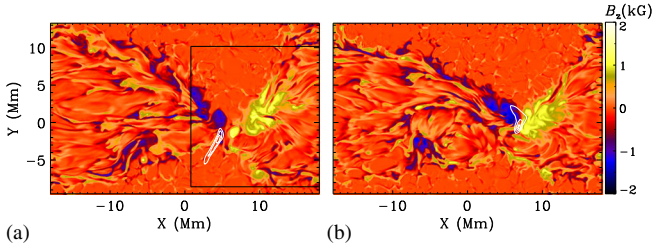

FIG. 3. Vertical component of the magnetic field, B_z, at $z = 0$ (shaded contours) (a) before and (b) after the collision of opposite polarities. Overlaid line contours (white) in (a) represent temperature contour levels at $z = 3.26$ Mm for values 90 000 K, 1M K, 1.2 MK whereas the respective temperature contour levels in (b) are at 90 000 K, 1 MK, 2.2 MK. This figure is available as an animation in the Supplemental Material [18].

above the region. This prevents the component polarities of the δ sunspot from separating during the rest of the evolution. Out of several flares we have been able to isolate only two strong ones, which can be located in Figs. 3(a) and 3(b) by the white colored contours of temperature at $z = 3.25$ Mm. The plasma is heated to a maximum temperature of 2.5 MK at this height where the average temperature is 54 000 K. The onset of the two flares can also be identified as the locations of peaks (dashed lines) in the temporal evolution of the magnetic energy, $\mathcal{E}_B$ [dashed-dotted line in Fig. 4(a)], inside a subvolume of the domain with $0 < z < 16.5$ Mm and the horizontal extent demarcated by a black square in Fig. 3(a). The flares are powered by the magnetic energy transported from the convection zone to the solar atmosphere. The rate of the magnetic energy input, or the Poynting flux, integrated over the faces of the same subvolume is, $\dot{\mathcal{E}}_{\rm PF} = \int c\mathbf{E} \times \mathbf{B} \cdot d\mathbf{S}/4\pi$ where, c is the speed of light, $\mathbf{E}$ is the electric field vector, and $d\mathbf{S}$ is the area element. The time evolution of $\dot{\mathcal{E}}_{\rm PF}$ is shown by the dashed-dotted line in Fig. 4(a). The maximum possible flare energy, $E^{\rm max}_{\rm flare}$ is related to the difference in magnetic energy, $\Delta\mathcal{E}_B$, after and before the flare as,

$$\Delta\mathcal{E}_B = -E^{\rm max}_{\rm flare} + \int_{\Delta t_{\rm flare}} \dot{\mathcal{E}}_{\rm PF} dt,$$

with $\Delta t_{\rm flare}$ being the duration of the flare. From Fig. 4 as well as the animation of Fig. 3, the flare occurring at $t = 167.5$ min lasts for 5 min and the one at $t = 197.2$ min lasts for 25 min. We estimate the magnetic energy release, $E^{\rm max}_{\rm flare}$ in the two cases to be 3.3×10^{29} ergs and 1.7×10^{30} ergs, respectively. The rate of energy release amounts to 1.1×10^{27} ergs s^{-1} in both cases, which agrees very well with the estimate made by Ref. [19] for a C-class flare that occurred on November 16, 2000. The magnetic energy dip at $t = 240.2$ min is due to the eruption of a highly twisted flux rope releasing at least 2.3×10^{30} ergs. We also observe good temporal correlation between the onset of energy release and bipolar reconnection jets appearing as pairs of maximum negative and positive values ($\sim \pm 270$ km s^{-1}) of vertical velocity [Fig. 4(b)].

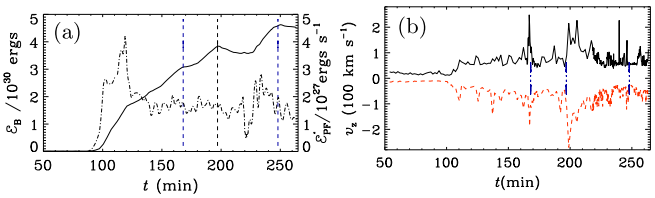

FIG. 4. Evolution of (a) magnetic energy, $\mathcal{E}_B$ (solid line), and $\dot{\mathcal{E}}_{\rm PF}$ (dashed-dotted line) and that of (b) maximum positive (solid line) and negative values (dashed line) of vertical velocity above the active region. The three vertical lines denote the times of the two flares and a flux rope eruption, respectively.

The magnetic field lines at the key moments before and during the onset of flaring are visualized in Fig. 5. Panel (a) illustrates the formation of a flux rope (FR-1) due to several reconnections above the large opposite polarities during the first of these flares at $t = 168.9$ min. Twenty-five minutes later an inverse-$\mathcal{S}$-shaped flux rope forms corresponding to a left-handed magnetic twist. The flux rope erupts later, denoted as EFR-1 in panel (c), possibly because it has been destabilized due to reconnections with the almost vertical magnetic field in the approaching positive polarity spot. The field lines, with red (blue) corresponding to upward (downward) velocity, clearly indicate the presence of a bipolar reconnection jet. These field lines pass through a current sheet, shown by a pink surface, with a thickness of $4\delta z$. The cusped reconnected field loops formed at this stage develop into a new sigmoidal flux rope (FR-2) at $t = 240.2$ min [panel (d)]. In panels (b)–(d), we note a *sigmoid-cusp-sigmoid* morphology transition over the region, also modeled by Ref. [20], and often observed in the coronal soft x rays above the source regions of homologous eruptions [21]. Here, the inverse-$\mathcal{S}$-shaped flux rope is formed due to reconnections inside the current sheet followed by the shearing photospheric foot point motions, flux

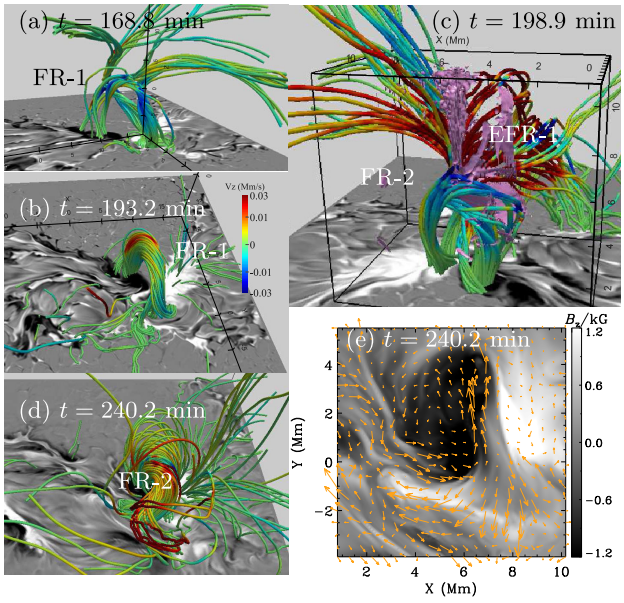

FIG. 5. (a)–(d) Magnetic field lines colored by the vertical velocity at times indicated to illustrate the formation and eruption of two flux ropes (FRs). The field lines traced in (c) pass through the current-layer isosurface (pink) with a value $J/B = 1/4\delta z$, where $cJ/4\pi$ is the current density, c being the speed of light. (e) Horizontal velocity vectors in the δ sunspot region. The grey shaded surface represents the vertical magnetic field at $z = 0$. A fly-by animation of panel (c) also including the subsurface structure of the δ sunspot is available as Supplemental Material [18]. Also available is an animation of the time evolution of the magnetic field in this region.

convergence, and cancellation; supporting earlier observations by Refs. [22,23] and simulations of Refs. [24,25], rather than subsurface flux tubes of Fig. 2(b) bodily emerging into the photosphere. Figure 5(e) shows strong shear at the polarity-reversal line between the spots which continuously pump twist and magnetic energy into the atmosphere in the form of a sustained Poynting flux $\sim 6 \times 10^8$ ergs s^{-1} cm^{-2} or 2×10^{27} ergs s^{-1} over the area of the box shown in Fig. 3. This value compares well with Fig. 2 of Ref. [26] where they calculate the Poynting flux for C-class flares producing NOAA AR 11560 within an area $\sim 145 \times 105$ Mm^2. After this time, the vertical component of the Poynting flux at $z = 0$ is clearly dominated by the shearing foot-point motions rather than subsurface flux emergence. We also note the formation and eruption of a dense and cool filamentlike structure above the δ sunspot region between $z = 2.3$–4.5 Mm as shown in Fig. 6(a). At the beginning of the filament formation, the dense region grows, supported by the tilted field loops underneath. At a later time during the filament evolution, the tilted field loops develop dips into which the plasma flows. This scenario is similar to 2.5-dimensional simulation of funnel prominence formation from an arcadelike geometry [27] but is distinct from the cavity prominences where dipped or concave field lines supporting the denser plasma preexist as part of an emerged flux rope in the corona [28]. The temperature inside the filament at $z = 2.75$ Mm is 1.1×10^5 K which is one third of the mean temperature in that layer. Hot plasma patches at 6.3×10^5 K exist close to the cooler filament. This phase separation of plasma into neighboring regions of hot and cold has long been attributed to the onset of thermal instability due to the radiative loss function [29,30]. Further, the evolution of these plasma condensations in long low-lying flux tubes is governed by the presence of both steady as well as impulsive heating just above the chromosphere [31]. We refer the readers to Ref. [32] for a detailed review on

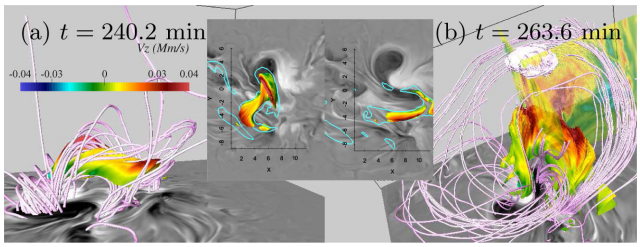

FIG. 6. Evolution of a dense filament over the δ sunspot. (a) DE = 21 surface shaded by vertical velocity at the time indicated. (b) The DE = 6 surface but 20 mins later when both the filament and the flux rope are erupting. The vertical planes are shaded by the vertical velocity to highlight the path of the erupting filament. The cloud in pink at the top has DE = 3.2. The insets in both panels show the surface, DE = 21, and line (cyan) contours with DE = 6 at $z = 2.3$ Mm superimposed on the top view of the photospheric magnetogram.

filament formation and structure. We define a quantity, DE, to describe the fractional density enhancement in the filament as $\rho/\bar{\rho}$, where $\bar{\rho} = \exp(\langle \ln \rho \rangle)$ with angular brackets denoting horizontal averaging. The region of plasma condensation has an inverse-$\mathcal{S}$ shape and the maximum density is 116 times the ambient or $\mathrm{DE}_{\mathrm{max}} = 116$. The total mass, at this stage, inside a volume bounded by the DE = 10 surface is 1.2×10^{13} kg. Panel (b) of Fig. 6 shows a part of the filament erupting at a speed of 50 km s^{-1} along with the twisted flux rope depicted in panel (d) of Fig. 5. The eruption speed is lower than observed, likely because the large viscosity and thermal diffusion used in this numerical simulation makes the conversion of the magnetic energy released to kinetic energy inefficient. The other possibility is the presence of a very weak preexisting magnetic field incapable of confining the flux rope [33,34] long enough to build sufficient nonpotential magnetic free energy in the system before its eruption. The magnetic free energy is a measure of the maximum energy available to drive eruptions. The larger the free energy, the faster may be the ejecta speeds. This may explain the absence of more energetic flares of class M and X in the simulated δ spot.

This numerical simulation started from a very primitive configuration, making no assumptions about the properties of subsurface flux tubes, demonstrates the formation of a δ sunspot from the collision of two or more young flux emerging regions developing in close vicinity. It is very similar to what is often seen in the solar photospheric magnetograms, e.g., the widely studied active region with NOAA number 11158. However, the two neighboring regions in the vicinity occur not by mere chance, but emerge almost simultaneously as they are part of the same initial subsurface structure. The collision leads to repeated flaring which according to us causes the pair to lock together throughout the evolution even though a major part of the component δ spots originate from topologically different flux tubes in the subsurface. This result validates the observational findings of Ref. [35] and Ref. [3] for δ sunspots from solar cycle 22. Another striking common feature of several observed δ sunspots, e.g., NOAA AR 11158, 10488 [36] and 10808 [37] and our simulation is the yin-yang structure of the interpenetrating positive and negative B_z in the late evolutionary phase [inset of Figure 6(b)]. Even though the treatment of the solar atmosphere is very simplified here, we believe it captures the essential physics of magnetic flux emergence and evolution into a flaring δ sunspot. There is scope for improvement, for instance by including self consistent Ohmic heating of the corona, ionization, and detailed radiative transfer; this will be our future work.

We thank two anonymous referees as well as O. V. S. N. Murthy for their comments which immensely helped improving the clarity of this Letter. The research leading to these results has received funding from the European

Research Council under the European Union's Seventh Framework Programmes (FP7/2007-2013) / ERC Grant agreement No. 291058 and (FP7/2007-2013) / F-CHROMA Grant agreement No. 606862. This research was also supported by the Research Council of Norway through the grant "Solar Atmospheric Modeling." The simulations were carried out on the NASA's Pleiades supercomputer under GID s1061. We have used the visualization software PARAVIEW for volume rendering and field line plotting.

*piyali.chatterjee@astro.uio.no

[1] H. Zirin, *Astrophysics of the Sun* (Cambridge University Press, Cambridge, England, 1988).
[2] F. Tang, Sol. Phys. **89**, 43 (1983).
[3] Z. Shi and J. Wang, Sol. Phys. **149**, 105 (1994).
[4] M. G. Linton, G. H. Fisher, R. B. Dahlburg, and Y. Fan, Astrophys. J. **522**, L1190 (1999).
[5] S. Takasao, Y. Fan, M. C. M. Cheung, and K. Shibata, Astrophys. J. **813**, 112 (2015).
[6] F. Fang and Y. Fan, Astrophys. J. **806**, 79 (2015).
[7] S. Toriumi, Y. Iida, K. Kusano, Y. Bamba, and S. Imada, Sol. Phys. **289**, 3351 (2014).
[8] D. Mitra, A. Brandenburg, N. Kleeorin, and I. Rogachevskii, Mon. Not. R. Astron. Soc. **445**, 761 (2014).
[9] V. Archontis and A. W. Hood, Astrophys. J. **674**, L113 (2008).
[10] V. Archontis and V. Hansteen, Astrophys. J. **788**, L2 (2014).
[11] D. J. Acheson, Sol. Phys. **62**, 23 (1979).
[12] Y. Fan, Astrophys. J. **546**, 509 (2001).
[13] A. Brandenburg and D. Schmitt, Astron. Astrophys. **338**, L55 (1998).
[14] P. Chatterjee, D. Mitra, M. Rheinhardt, and A. Brandenburg, Astron. Astrophys. **534**, A46 (2011).
[15] https://github.com/pencil-code/.
[16] G. Guerrero and P. J. Käpylä, Astron. Astrophys. **533**, A40 (2011).
[17] N. J. Nelson, B. Brown, A. S. Brun, M. Meisch, and J. Toomre, Astrophys. J. **739**, L38 (2011).
[18] See Supplemental Material at http://link.aps.org/supplemental/10.1103/PhysRevLett.116.101101 for model details.
[19] H. Isobe, H. Takasaki, and K. Shibata, Astrophys. J. **632**, 1184 (2005).
[20] P. Chatterjee and Y. Fan, Astrophys. J. **778**, L8 (2013).
[21] S. E. Gibson, L. Fletcher, G. Del Zanna, C. D. Pike, H. E. Mason, C. H. Mandrini, P. Dmoulin, H. Gilbert, J. Burkepile, T. Holzer, D. Alexander, Y. Liu, J. Nitta, N. Qiu, B. Schmieder, and B. J. Thompson, Astrophys. J. **574**, 1021 (2002).
[22] S. F. Martin, *Dynamics of Quiescent Prominences*, edited by V. Rudjak and E. Tandberg-Hanssen, Vol. 363 (Springer-Verlag, Berlin, 1990).
[23] V. Gaizauskas, J. B. Zirker, C. Sweetland, and A. Kovacs, Astrophys. J. **479**, 448 (1997).
[24] A. A. van Ballegooijen and P. C. H. Martens, Astrophys. J. **343**, 971 (1989).
[25] P. C. Martens and C. Zwaan, Astrophys. J. **558**, 872 (2001).
[26] P. Vemareddy, Astrophys. J. **806**, 245 (2015).
[27] C. Xia, P. F. Chen, and R. Keppens, Astrophys. J. **748**, L26 (2012).
[28] V. Archontis and A. W. Hood, Astron. Astrophys. **537**, A62 (2012).
[29] E. N. Parker, Astrophys. J. **117**, 431 (1953).
[30] G. B. Field, Astrophys. J. **142**, 531 (1965).
[31] J. T. Karpen and S. K. Antiochos, Astrophys. J. **676**, 658 (2008).
[32] D. H. Mackay, J. T. Karpen, J. L. Ballester, B. Schmieder, and G. Aulanier, Space Sci. Rev. **151**, 333 (2010).
[33] Y. Fan, Astrophys. J. **719**, 728 (2010).
[34] G. Aulanier, T. Török, P. Démoulin, and E. E. DeLuca, Astrophys. J. **708**, 314 (2010).
[35] H. Zirin and M. Liggett, Sol. Phys. **113**, 267 (1982).
[36] J. Liu and H. Zhang, Sol. Phys. **234**, 21 (2006).
[37] H. Li, B. Schmieder, M. T. Song, and V. Bommier, Astron. Astrophys. **475**, 1081 (2007).